JOURNAL OF GEOPHYSICAL RESEARCH, VOL. 100, NO. D12, PAGES 26,247–26,261, DECEMBER 20, 1995

Radiative smoothing in fractal clouds

Alexander Marshak,[1] Anthony Davis,[1] Warren Wiscombe, and Robert Cahalan

Center, Climate and Radiation Branch, NASA Goddard Space Flight Greenbelt, Maryland

Abstract. Spectral and structure function analyses are used to study the smoothness properties of the radiation fields for stratiform clouds whose horizontally fluctuating extinction fields are modeled with multiplicative cascades. Models of this type are "scale invariant," meaning that their two-point statistics obey power laws in the scale parameter. The independent pixel approximation (IPA) treats each pixel as a plane-parallel layer and yields scale-invariant albedo and radiance fields with the same exponents as the associated optical depth field. This is not the case with exact Monte Carlo (MC) results for which we confirm the existence of a characteristic "radiative smoothing" scale η. For scales larger than η, IPA and MC reflectance fields fluctuate together, and the IPA can be invoked to infer optical depths from measured radiances. We use a multifractal characterization of structure functions to assess the performance of such retrievals. For scales smaller than η, MC fields are much smoother than their IPA counterparts, and IPA-based retrievals of the underlying optical depth field are unreliable. The scale break location η has been found to be closely related to the characteristic size $\langle\rho\rangle$ of the "spot" of multiply scattered light excited by illumination with a narrow beam, the random variable ρ being the horizontal distance between photon entry and exit points. New analytical arguments are presented for thick homogeneous media showing that $\langle\rho\rangle \approx h[(1-g)\tau]^{-1/2}$, given the cloud's optical (τ) and geometrical (h) thicknesses (g is the asymmetry factor); this result is shown to hold numerically for fractal cloud models too. An improved "nonlocal" IPA is defined as the convolution product of the IPA field with a gamma-type smoothing kernel dependent on $\langle\rho\rangle$.

1. Introduction

Statistically realistic horizontal distributions of cloud liquid water can be simulated [*Cahalan et al.*, 1994a] by using fractal models adapted from the highly successful cascade phenomenology of turbulence [*Meneveau and Sreenivasan*, 1987]. Mathematically speaking, these models are continuous but nowhere differentiable stochastic processes, and their main property is scale invariance: their two- and more-point statistics follow power laws in the scale parameter, e.g., the distance between the two points considered in an autocorrelation function.

Intuitively, we expect radiation fields in clouds to be smoother than the liquid water fields, hence extinction ones, because of photon transport effects. The Landsat cloud scenes studied by *Cahalan and Snider* [1989] and others [*Lovejoy et al.*, 1993; S. Gollmer, private communications, 1994; H. Barker, private communications, 1995] are not scale invariant over the full range of observable scales (almost 100 km to less than 100 m). Rather, they found that the fluctuations of the radiance field follow those of the liquid water column at the largest scales (greater than 200–500 m) but, at smaller scales, it exhibits much smoother behavior. Hence a scale break in the radiance wavenumber spectrum was reported, meaning that there is a characteristic scale that separates two distinct scaling regimes.

The large-scale regime is well described radiatively by the "independent pixel" approximation (IPA), which uses plane-parallel radiative transfer theory locally, ignoring net horizontal photon transport. The IPA is also applied implicitly in all current cloud remote sensing applications where the radiation fields are used to infer optical and physical properties such as optical depth and effective droplet radius [*Nakajima and King*, 1990]. In some cases [*Harshvardan et al.*, 1994; *Barker and Liu*, 1995], IPA retrievals have been applied down to very small scales, such as the 30–60 m in Landsat imagery; we will argue further on that this is not justified in general.

The Landsat scale break and its relation to the breakdown of the IPA is investigated elsewhere [A. Davis, A. Marshak, R. Cahalan, and W. Wiscombe (Horizontal radiative fluxes in stratocumulus and the Landsat scale-break, submitted to *Journal of Atmospheric Sciences*, 1995)]. In the present study we address two important problems left outstanding. (1) Can the computationally fast IPA technique be improved without resorting to costly Monte Carlo (MC) schemes? (2) Even restricting the IPA to large enough scales, how well does it retrieve optical thicknesses, statistically speaking?

The plan of this paper is as follows. In the next section we recall some general aspects of spectral and structure function analysis. Section 3 describes our fractal cascade models for horizontal distributions of optical thickness and some of their scaling properties. In section 4 we describe two numerical methods for computing radiation fields emerging from inhomogeneous clouds: the IPA and Monte Carlo simulation. In section 5 we characterize horizontal photon transport in homogeneous and fractal media by estimating the size of the spot resulting from localized illumination. As an application

[1] Also at Science Systems and Applications, Inc., Lanham, Maryland.

Paper number 95JD02895.
0148-0227/95/95JD-02895$05.00

of these results we derive in section 6 an improved "nonlocal" IPA and use it to revisit the Landsat scale break problem. In section 7 we use structure function analysis to assess the performance of IPA-based retrievals of optical thickness fields. Finally, section 8 summarizes our results. Appendix A explains the less standard aspects of our numerical techniques. In Appendix B a boundary value problem is set up and solved to determine the average numbers of scatterings suffered by reflected and transmitted photons.

2. Statistical Preliminaries

2.1. Scale Invariance and Energy Spectra

In this study we focus on stochastic cloud models and related data which are scale invariant: their statistical properties follow power laws in scale r. For the energy (or wavenumber) spectrum we can write

$$E(k) \propto k^{-\beta} \quad k = 1/r \tag{1}$$

over a large range of r. The spectral exponent β in (1) can be used to distinguish stationary ($\beta < 1$) and nonstationary ($\beta > 1$) scale-invariant stochastic processes [Davis *et al.*, 1994]. But here we are interested in the spectral exponent as an indirect indication of smoothness properties of stochastic processes: among two nonstationary scale-invariant processes with $1 > \beta_1 > \beta_2$ the one with larger spectral exponent is smoother.

If there are two well-established scale-invariant regimes, each of which is over a considerable range of scales, we have one characteristic scale. The transition in power law behavior from $k^{-\beta_1}$ to $k^{-\beta_2}$ is called a scale break. The characteristic scale where the scale break occurs has an important physical meaning: it pinpoints a change in the physical processes that govern the variability at the corresponding scales.

2.2. Structure Functions

Besides spectral analysis we will rely on "structure functions" to study the smoothing properties of radiative transfer. In this subsection we discuss power law structure functions in general terms, starting with the Hölder exponent.

Smoothness properties of any continuous function f can be characterized by its Hölder exponent a:

$$|f(x+\Delta x) - f(x)| \le \text{const}\, |\Delta x|^a \quad 0 < a \le 1. \tag{2}$$

The larger a is, the smoother f is. The extreme case $a = 1$ corresponds to the class of differentiable functions.

For a stochastic process ϕ we can define H_1, the statistical counterpart of a, as the scaling exponent for the first moment of its absolute increments, $|\Delta\phi(x,r)| = |\phi(x+r) - \phi(x)|$ with $r > 0$:

$$\langle |\Delta\phi(x,r)| \rangle \sim r^{H_1} \quad 0 \le H_1 \le 1, \tag{3}$$

where angle brackets denote ensemble averaging. Exponent H_1 is related to the fractal dimension D of the graph of $\phi(x)$, viewed as a (random) geometrical object in two-dimensional space by *Mandelbrot* [1977],

$$D = 2 - H_1. \tag{4}$$

The fractal dimension D lies between unity (a rectifiable curve) and 2 (a measurable area), inclusive. Then $H_1 = 2-D$, the codimension of the graph, goes from zero (a jumpy, discontinuous process) to unity (a differentiable one) and thus provides a direct and natural measure of smoothness.

In general, structure functions generalize equation (3) by requiring that, for all moments of real order q,

$$\langle |\Delta\phi(x,r)|^q \rangle \sim r^{\zeta(q)}, \tag{5}$$

where $\zeta(1) = H_1$. The implicit hypothesis that the prefactors in (5) depend only weakly on q implies that the function $\zeta(q)$ is concave ($\zeta''(q) \le 0$) with $\zeta(0) = 0$ [*Parisi and Frisch*, 1985]; if, furthermore, the moments in (5) are finite, it can be shown [*Frisch*, 1991; *Marshak et al.*, 1994] that $\zeta(q)$ is nondecreasing. "Simple" scaling (or monoscaling) means that $\zeta(q)$ is a linear function $\zeta(q) = q\zeta(1) = qH_1$; in this case, H_1 is the only quantity needed for a two-point statistical description of the stochastic process ϕ. The classic example of simple scaling is fractional Brownian motion [*Mandelbrot*, 1977]. If $\zeta(q)$ is not linear, the stochastic process ϕ exhibits multiscaling or "multifractality" [*Parisi and Frisch*, 1985] or "multiaffinity" [*Viscek and Barabási*, 1991], and the whole family of exponents $\zeta(q)$ is required to describe ϕ statistically.

Finally, *Monin and Yaglom* [1975] discuss a Wiener-Khinchine relation between the second-order ($q = 2$) structure function and the energy spectrum $E(k)$. If (1) and (5) apply simultaneously over the same range of scales, then

$$\beta = \zeta(2) + 1 > 1. \tag{6}$$

3. Realistic Cloud Models

3.1. Multiplicative Cascades

Imagine a substance uniformly distributed with density ϕ_0 over the unit interval. The interval is subdivided into two intervals of size 1/2, and a certain amount of mass is randomly redistributed between these subintervals; this is equivalent to multiplying ϕ_0 on one side by a factor $2p$, $0 \le p \le 1/2$, and on the other by $2(1-p)$. At the next step of the construction, each of the subintervals is divided into two parts of equal size, and the same process is repeated. Proceeding iteratively, there are exactly $N = 2^n$ subintervals at the nth cascade step. Because of the conservative nature of the redistribution procedure the average density remains equal to ϕ_0.

In general, a multiplicative cascade model at nth level, ϕ_n, is represented by a product of n nonnegative identically distributed random numbers (weights) W, i.e.,

$$\phi_n = \phi_0 \prod_{i=1}^{n} W_i \quad n=1,2,\ldots, \tag{7}$$

A simple example is *Meneveau and Sreenivasan*'s [1987] "p model" where the W values are either $2p$ or $2(1-p)$, with equal probability irrespective of the cascade step (see Figure 1a for an illustration); by construction it obeys

$$\langle \phi_n \rangle = \frac{1}{N} \sum_{m=1}^{N} \phi_n(x_m) = \phi_0, \quad N=2^n, \quad n=1,2,\ldots . \tag{8}$$

Cascade models (7) are scale invariant: their statistics follow power laws in scale r. Thus their energy spectra are defined by spectral exponents β in (1). For example, the p model has [*Meneveau and Sreenivasan*, 1987]

$$\beta = 1 - \log_2[1+(1-2p)^2]. \tag{9}$$

In equation (9), $0 < \beta < 1$ characterizes the "singularity" of the

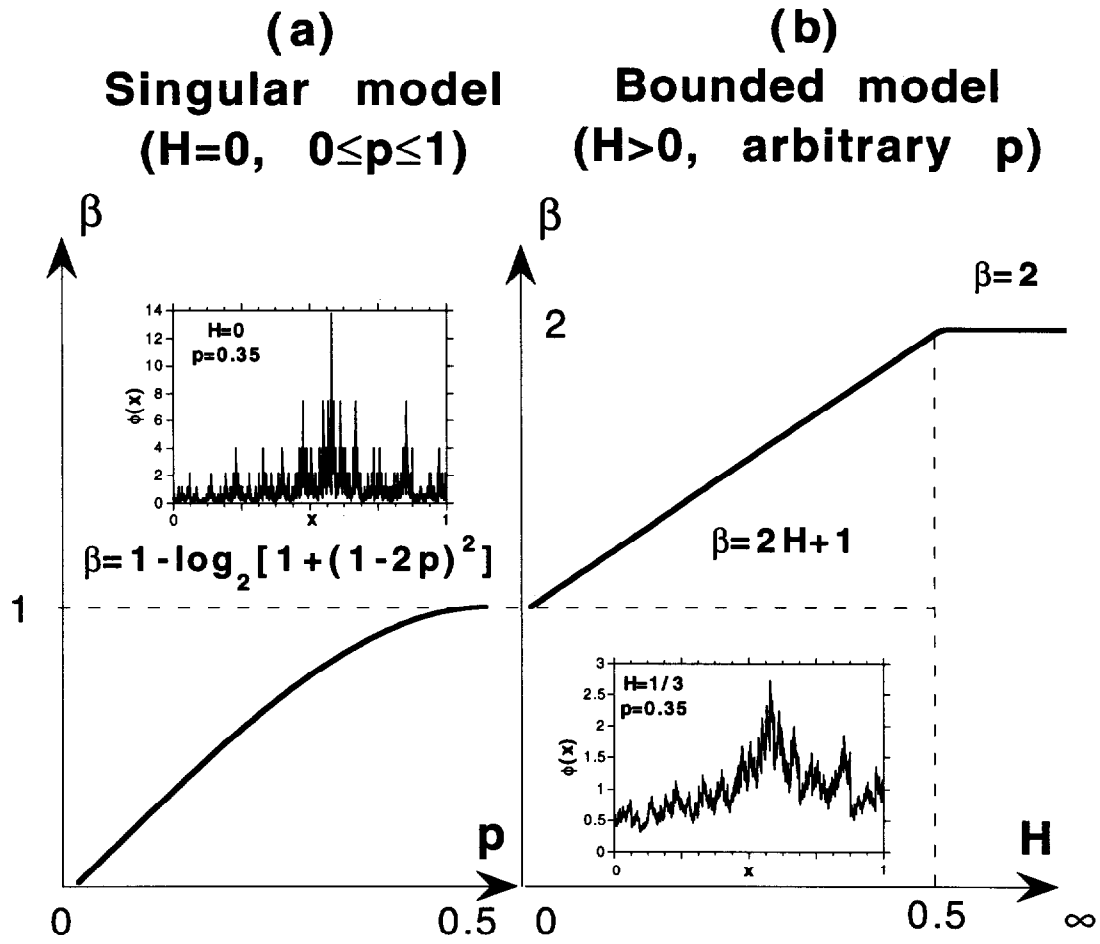

Figure 1. Spectral exponents for "p model" and "bounded" cascades. (a) The singular p model ($H = 0$) where β is determined by p (see (9)); the inset shows the $p = 0.35$ case that best fits *Meneveau and Sreenivasan*'s [1987] turbulence data. (b) The bounded model ($H > 0$) where β is independent of p and defined by (12); the inset shows $H = 1/3$, $p = 0.35$ case which fits *Cahalan*'s [1994] afternoon liquid water path data.

p model. Indeed, if the weights W do not converge to 1 as $n \to \infty$, $\phi_n \to 0$ almost everywhere as the cascade proceeds but, since $\langle \phi_n \rangle = \phi_0$ for all n by definition, ϕ_n must approach infinity on some sparse subset of points (technically, of vanishing Lebesgue measure as $n \to \infty$). Below we describe one way of "taming" this singularity enough to produce realistic cloud models with bounded liquid water cascades. For scale-invariant models smoothing is equivalent to increasing β.

3.2. Bounded Cascade Models

We now require the weights to converge to 1 as the cascade proceeds. Following *Cahalan et al.* [1994a] (but with different notations), we choose weights

$$W_n = 1 \pm (1-2p)/2^{(n-1)H} \quad 0 \le p \le 1/2 \quad H \ge 0. \quad (10)$$

This choice is empirical and is justified mainly by its success in simulating observed liquid water data. If $H = 0$, we retrieve the singular p model with $\beta < 1$ defined by equation (9). If $H > 0$, $W_n \to 1$ as $n \to \infty$, and the cascade model is bounded; i.e., there exist $\phi_{\min}$ and $\phi_{\max}$ such that [*Cahalan et al.*, 1994a]

$$0 < \phi_{\min} \le \lim_{n\to\infty} \phi_n \le \phi_{\max} < \phi_0 \exp\left[\frac{2^H (1-2p)}{2^H - 1}\right] < \infty. \quad (11)$$

The energy spectrum scales as (1), and in the limit of infinite number of cascade steps the spectral exponent β is [*Cahalan et al.*, 1994a; *Marshak et al.*, 1994],

$$1 < \beta = \min\{2H, 1\} + 1 \le 2. \quad (12)$$

Figure 1 illustrates the continuity between (9) and (12) and gives two examples of singular and bounded models which have spectral exponents $1-\log_2 1.09 \approx 0.88$ and 5/3, respectively.

The properties of structure functions (cf. section 2.2) for the bounded cascade model were studied by *Marshak et al.* [1994]. It was found that in the limit of infinite number of cascades, $H_1 = \min\{H,1\}$. Generally speaking, we have

$$\zeta(q) = qH \quad 0 \le q \le 1/H$$
$$\zeta(q) = 1 \quad 1/H \le q \le \infty; \quad (13)$$

so (12) follows from (6) and (13). Thus the bounded cascade model, while multifractal, cannot be distinguished from monoscaling fractional Brownian motion (which has $\zeta(q) = qH$) for moments smaller than $q = 1/H$.

In summary, bounded cascade models belong to the class of stochastically continuous (with Hölder exponent

$H_1 = \min\{H,1\}$) multiscaling models with stationary increments.

3.3. Choice of Parameters for the Cloud Model

To choose the parameters of the horizontal distribution of vertical optical thickness, τ, we will use the characteristics of vertically integrated liquid water path, *LWP*, as measured in marine stratocumulus (Sc) by *Cahalan and Snider* [1989]. Assuming that the effective droplet radius, r_{eff}, is constant, we obtain the simple linear relation, $\tau = 1.5LWP/r_{\text{eff}}$, where *LWP* is in gram per square meter and r_{eff} is in micrometers [e.g., *Stephens*, 1976]; in this case, τ has the same statistical properties as *LWP*.

Cahalan and Snider found that the wavenumber spectrum $E(k)$ of *LWP* in marine Sc follows a $k^{-5/3}$ power law from over 400 km to about 500 m. This immediately implies $H = 1/3$ for the bounded cascade model, from equation (12), which, however is exact only for an infinite number of cascade steps [*Marshak et al.*, 1994]. To simulate the energy spectrum with a limited 10-cascade-step bounded model, we need a slightly larger H, namely, $H = 0.38$; this gives us spectral exponent $\beta \approx 1.6$, while $H = 1/3$ would give about 1.5. The model's remaining parameter p (called "variance parameter," since it controls the width of distribution of *LWP*) was estimated by *Cahalan et al.* [1994a] to have a diurnal average $p = 0.25$; according to *Cahalan* [1994], p varies from 0.20 in the morning to 0.35 in the afternoon owing to the well-known diurnal cycle of marine Sc.

In most of our numerical simulations we set the mean optical depth $\phi_0 = \tau_0 = 13$ corresponding to values of r_{eff} and *LWP* for Sc of 10 μm and 90 g/m^2, respectively. The cloud thickness $h = 0.3$ km is also typical for marine Sc. This gives us a mean extinction coefficient $\sigma_{\text{mean}} = 13/0.3 = 43$ km^{-1}. To emulate a large horizontal extension, we apply cyclical boundary conditions in the following radiative transfer computations.

Let us summarize the main assumptions of our cloud model. First, we assume that clouds are vertically homogeneous; thus the local optical depth τ depends only on horizontal coordinates x, or x and y. It is well known that even in marine Sc—the closest of any cloud type to have plane-parallel geometry—most liquid water is concentrated in the upper layers of a cloud; however, in stratus decks, reflectance is only weakly sensitive to vertical inhomogeneity [*Li et al.*, 1994]. Second, we assume that both upper and lower cloud boundaries are horizontal planes; this is justifiable for marine Sc. Next we use the same phase function and single-scattering albedo everywhere, except that extinction varies spatially through τ; this is equivalent to assuming constant effective droplet radius and variable liquid water content. Finally, we take liquid water, hence τ, to be scale invariant down to the pixel size; below this inner scale the model is assumed homogeneous. Thus our fractal model simulates the internal distribution of liquid water in Sc clouds, and our results are limited to this type of clouds.

4. Radiative Transfer in Fractal Clouds

4.1. The Independent Pixel Approximation

The independent pixel approximation for radiative transfer in horizontally variable clouds treats each cloud pixel as an independent plane-parallel medium. Thus the resulting single-pixel response, say, albedo $R_{\text{IP}}(\tau_i)$ ($i = 1,\ldots,N_p$), depends on the vertical optical depth τ_i of this pixel but not on the optical depth of neighboring pixels [*Cahalan*, 1989; *Cahalan et al.*, 1994a]. (We assume that other parameters, such as the asymmetry factor g, are held constant.) In other words, the IPA ignores any net horizontal photon transport; as a result, the domain-averaged albedo,

$$\langle R_{\text{IP}}(\tau)\rangle = \frac{1}{N_p}\sum_{i=1}^{Np} R_{\text{IP}}(\tau_i) \tag{14}$$

where N_p is the total number of pixels, depends only on the one-point probability distribution of the optical depth field and neglects the effects of all the two- and more-points statistics discussed in section 2.

For climate and remote sensing purposes, we are interested in both fluxes (mostly for climate) and radiances (mostly for remote sensing). To compute $R_{\text{IP}}(\tau)$ and the corresponding transmitted flux $T_{\text{IP}}(\tau)$, one can use a two-stream approximation which, in the case of conservative scattering, gives [*e.g., Lenoble*, 1985]

$$R_{\text{IP}}(\tau;\theta_0,g) = 1 - T_{\text{IP}}(\tau;\theta_0,g),\quad T_{\text{IP}}(\tau;\theta_0,g) = \frac{1}{1+\left(\frac{1-g}{2\cos\theta_0}\right)\tau} \tag{15}$$

where θ_0 is the solar zenith angle. A more accurate analytic expression for reflection by a conservatively scattering plane-parallel medium is given by *Cahalan et al.* [1994a]. If even more accuracy is needed, $R_{\text{IP}}(\tau;\theta_0,g)$ can be computed with a general purpose plane-parallel radiative transfer code such as DISORT [*Stamnes et al.*, 1988]. We use the latter to compute single-pixel nadir radiance $I_{\text{IP}}(\tau;\theta_0,g)$, emitted vertically upward from the top boundary.

Although the IPA formula is nonlinear in τ (see equation (15)), the albedo field it generates has almost the same scaling properties as the original optical depth field. Figure 2a shows first-order structure functions defined by equation (3) for three fields: optical depth, albedo, and nadir radiance. The slopes H_1 in Figure 2*a* are virtually identical for all three quantities. Energy spectra $E(k)$ (Figure 2b) confirm the scaling of the IPA radiation field. While the spectral exponent β of the optical depth field gives the value of 1.58 (theoretically 5/3 if an infinite number of cascade steps is used), the resulting IPA fields show $\beta = 1.60$. Since the IPA ignores any interpixel (i.e., horizontal) photon transport, it does not smooth the original optical depth field. In order to study the smoothing effect of radiative transfer we must use the more accurate but time-consuming Monte Carlo method.

4.2. Monte Carlo Methods Versus Independent Pixel Approximations

In Appendix A we discuss the lesser-known techniques used in our forward Monte Carlo (MC) code. In particular, we implemented the "maximal cross-section" variance reduction technique [*Marchuk et al.*, 1980], a trick that makes the computer time almost insensitive to the variability of the optical depth field and to the number of cells and number of dimensions.

Figure 3 illustrates the outcome of both IPA and MC methods applied to a two-dimensional bounded model, a straightforward generalization of the one-dimensional case described in section 3.2; it had seven cascade steps,

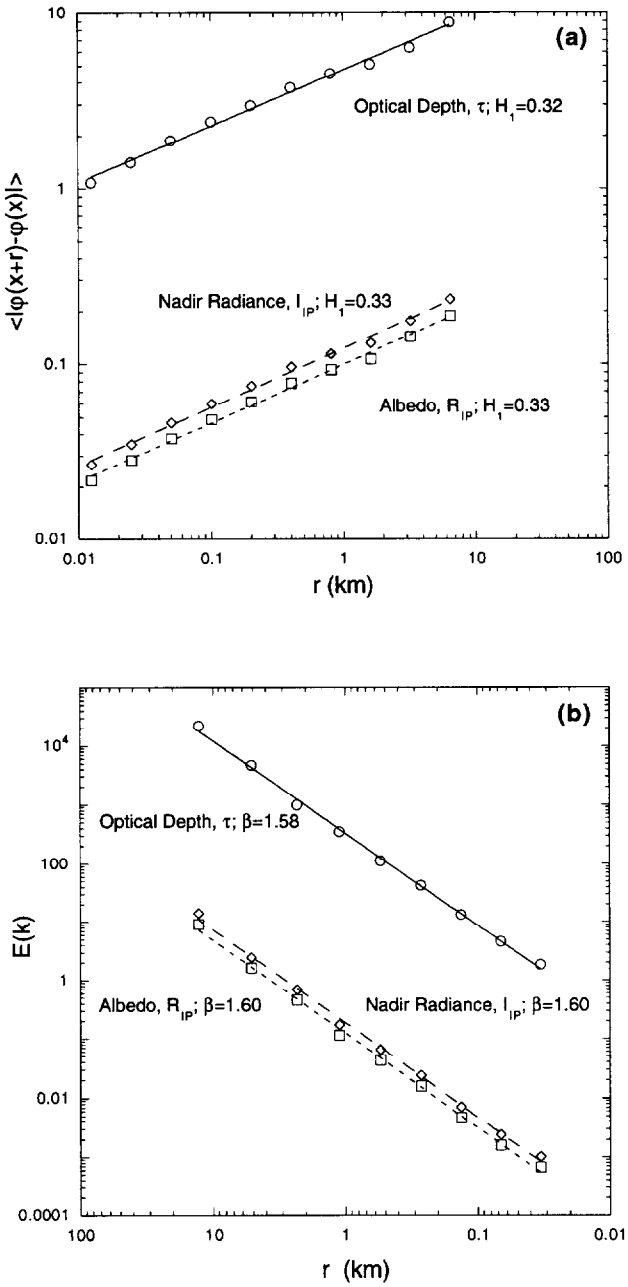

Figure 2. First-order structure functions and energy spectra for cloud optical depth and reflectivity. (a) First order structure function versus scale r for vertical optical depth τ, IPA nadir radiance I_{IP}, and IPA albedo R_{IP} fields ($\varphi(x)$ stands for any one of these quantities). A one-dimensional fractal cascade cloud model with 10 cascade steps, $H = 0.38$, $p = 0.35$, and $\langle\tau\rangle = 13$ was used with optical parameters being Sun angle $\theta_0 = 22.5°$ and asymmetry factor $g = 0.85$; R_{IP} is from equation (15), I_{IP} is from DISORT using a *Henyey and Greenstein* [1941] phase function. (b) Same as in Figure 2a but for energy spectra $E(k)$ where wavenumber $k = 1/r$. To estimate the spectral exponent β, $\log_2 E(k)$ is fitted to a power law by least squares. If all wavenumbers are used, the fit is dominated by large wavenumbers; to make all wavenumbers contribute equally, $E(k)$ and k are averaged by octaves.

altogether $(2^7)^2 = 16{,}384$ pixels, and an average cloud optical depth, $\langle\tau\rangle = 13$ (see *Cahalan* [1994] and *Marshak et al.* [1995] for visualizations). Pixels range in optical depth from ≈1.4 to ≈65 (cf. (11)). In equation (15), $R_{IP}(\tau)$ is a concave function of τ; it can then be shown [*Jensen*, 1906] that $\langle R_{IP}(\tau)\rangle < R_{IP}(\langle\tau\rangle) = R_{PP}$, this last quantity being the deterministic prediction of plane-parallel theory, ignoring the internal structure. For the albedo of marine Sc, *Cahalan et al.* [1994a] found a significant "plane-parallel bias," $R_{PP}-\langle R_{IP}\rangle$, which is typically around 10-15% of R_{PP} (≈8% in Figure 3). In sharp contrast the differences between $\langle R_{IP}\rangle$ and $\langle R_{MC}\rangle$, the latter being the domain average Monte Carlo flux, is relatively small, around 1%. Small dots in Figure 3 show all the pixel values of R_{MC}. We can see dramatic differences between R_{MC} and R_{IP} in individual pixel albedo; some of them are as big as 50% of $R_{IP}(\tau)$. Several values of R_{MC} even exceed unity, meaning that more energy leaves the corresponding pixel than enters it. This can only be explained in terms of interpixel interactions.

As another illustration of the difference between individual pixel albedos calculated by IPA and MC, Figure 4a shows both the optical depth and the IPA and MC fields plotted against horizontal distance x, for Sun at 22.5°. While both albedos show the same domain average of ≈0.5, there are large differences in individual pixels. As noted in section 4.1, there is a direct relation between the IPA reflectivity and local optical depth; the horizontal fluctuations of $R_{IP}(x)$ follow those of optical depth, showing no smoothing effect. By contrast, $R_{MC}(x)$ shows considerable smoothing. To better illustrate the smoothness of $R_{MC}(x)$, Figure 4b shows a 1-km fragment of Figure 4a, consisting of 80 pixels, each 12.5 m wide; the very small numerical noise in the MC signal is now apparent, showing that $R_{MC}(x)$ is compatible with a differentiable function, plus noise.

5. Horizontal Photon Transport in Homogeneous and Fractal Media

5.1. Average Number of Scatterings for Reflected and Transmitted Photons

In this subsection we study the average number of scatterings in the radiative diffusion approximation. Consider a plane-parallel conservative ($\varpi_0 = 1$) medium of geometrical thickness h with imbedded diffuse sources uniformly distributed on the plane $z = z^*$; we can set up the following boundary value problem [*Case and Zweifel*, 1967]:

$$\begin{cases} -D\dfrac{d^2J}{dz^2} = \sigma\delta(z-z^*), & 0 \le z, z^* \le h \\ \left[J - \chi\dfrac{dJ}{dz}\right]_{z=0} = \left[J + \chi\dfrac{dJ}{dz}\right]_{z=h} = 0 \end{cases} \tag{16}$$

for the normalized photon density $J(z)$. In equation (16), $D = [3(1-g)\sigma]^{-1}$ is the diffusion coefficient where the extinction coefficient $\sigma = \tau/h$ and g is the asymmetry factor; χ is the "extrapolation" length, to which we assign the customary value of $2D$.

The solution of (16) is the Green's function:

$$G(z,z^*) = \frac{\sigma}{D(h+2\chi)}\begin{cases}(z+\chi)(\chi-z^*+h), & 0\le z\le z^* \\ (z^*+\chi)(\chi-z+h), & z^*<z\le h\end{cases} \quad 0 \le z^* \le h. \tag{17}$$

Based on a time-dependent counterpart of this boundary-value problem, Appendix B shows that the average number of scatterings $N(\tau,g)$ is proportional to the integral of $G(z,z^*)$ over z from 0 to h. The result is

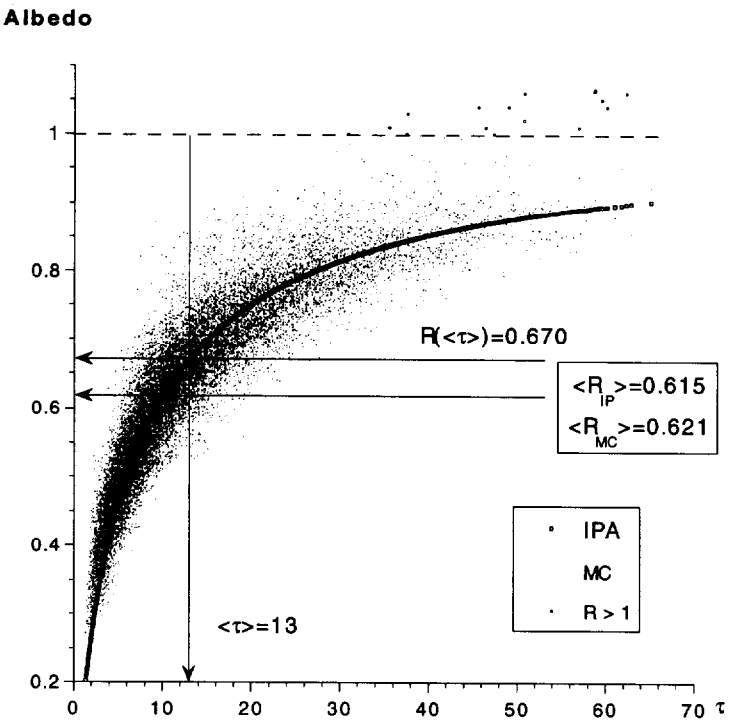

Figure 3. IPA and MC albedos versus optical depth. The horizontal distribution of the optical depth is simulated by a two-dimensional bounded model [*Marshak et al.*, 1995] with $\langle\tau\rangle = 13$ and $H = 1/3$. Geometrical thickness is 300 m, and the horizontal grid size is 128 x 128 with 50-m pixels—hence an outer scale of 6.4 km (larger horizontal scales are accommodated by applying cyclical boundary conditions). The Sun angle θ_0 is 60° and scattering is anisotropic according to a Henyey-Greenstein phase function with $g = 0.85$. The thick line gives the range of IPA albedos using *Cahalan et al.*'s [1994a] parameterization. The $128^2 = 16{,}384$ dots are the outcome of a MC simulation with 10^8 photons; a few of these albedos (highlighted on the plot) exceed unity. Plane-parallel theory for $\tau = \langle\tau\rangle$ gives an overestimated albedo of 0.670, while domain-averaged MC and IPA albedo give close results: 0.621 and 0.615, respectively.

$$N(\tau,g) \sim \tau \quad \text{for reflected photons} \qquad (18)$$

$$N(\tau,g) \sim (1-g)\,\tau^2 \quad \text{for transmitted photons.}$$

Notice that the average number of scatterings for reflected (albedo-contributing) photons is independent of the asymmetry factor g. A linear response in τ is often mapped to optically thin situations [e.g., *Rybicki and Lightman*, 1979, p. 36]. This is not the case here; in fact, equation (16) is valid only if $(1-g)\,\tau \gg 1$, in order to apply the diffusion approximation.

The above derivation of (18) relies heavily on the homogeneity assumption of standard plane-parallel theory. However, our numerical results show that the same scaling holds approximately for bounded cascade models using $\langle\tau\rangle$ in place of τ, at least for the physically reasonable range of optical thicknesses we explored (up to $\langle\tau\rangle = 64$, hence $\max_x\{\tau\} \approx 300$). Figure 5 illustrates the average number of scatterings $N(\tau,0)$ for both homogeneous and a bounded cascade model having the same optical depth on average; to enhance photon diffusion, isotropic diffuse illumination and isotropic scattering were used. Plotted on log-log axes, $N(\tau,0)$ exhibit straight lines with slopes close to 1 for reflected photons and close to 2 for their transmitted counterparts, as predicted by (18). It is remarkable that these relationships hold down to $\tau \approx 4$ in spite of being derived for large τ; the effect of anisotropic scattering is simply to displace the onset of the diffusion regime to slightly higher τ values. It is notable that for reflected photons the average number of scatterings almost coincides for both models while for transmitted photons this number is much smaller in the fractal case.

5.2. Characteristic Spot Size

In this section we study distributions of the random number $\rho = [(x_{out}-x_{in})^2+(y_{out}-y_{in})^2]^{1/2}$ where $\boldsymbol{x}_{in} = (x_{in},y_{in},0)$ is the photon's random entry point at cloud top and $\boldsymbol{x}_{out} = (x_{out},y_{out},0)$ or $\boldsymbol{x}_{out} = (x_{out},y_{out},h)$ is the photon's exit point if reflected or transmitted, respectively. The first moment of ρ, denoted $\langle\rho\rangle$, characterizes the size of the spot resulting from illumination by a narrow beam.

We first assume that our photons travel in a homogeneous plane-parallel medium of optical thickness τ and geometrical depth h, the scattering being conservative with an asymmetry factor g. To estimate $\langle\rho\rangle$, we will use an analogy with Brownian motion. Unlike for photon trajectories, scattering in Brownian motion is isotropic. However, it can be shown that the total number of "effectively isotropic" scatterings is $(1-g)N(\tau,g)$ on average, and that the rescaled (or "transport") mean free path is

$$l_t = \frac{h}{(1-g)\tau}. \qquad (19)$$

(See A. Davis, A. Marshak, R. Cahalan, and W. Wiscombe (Horizontal radiative fluxes in stratocumulus and the Landsat

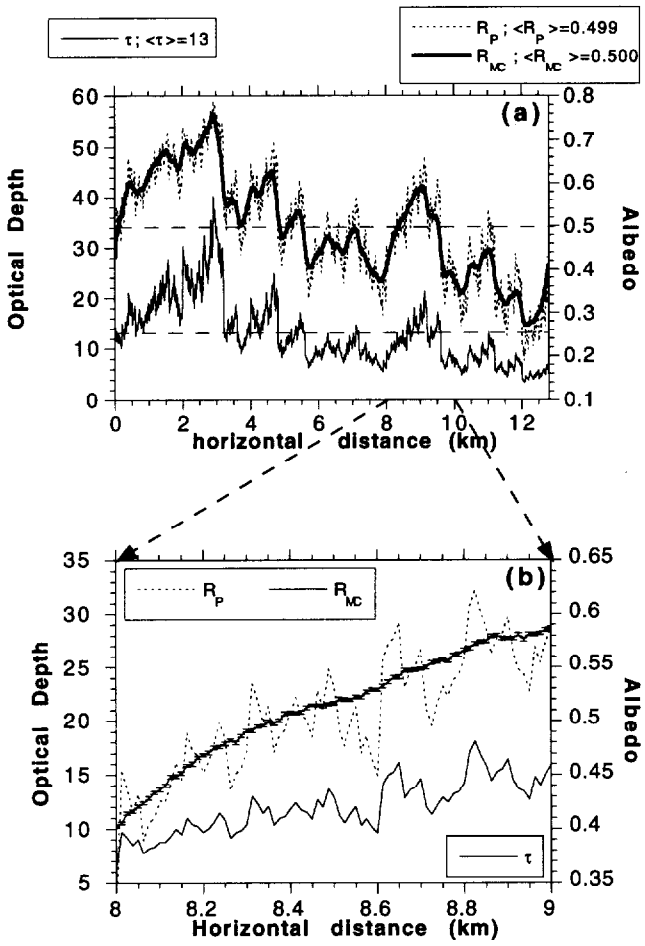

Figure 4. Horizontal variations of optical depth, IPA, and MC albedos in the x direction. (a) Parameters and model are the same as in Figure 2 for the IPA calculations; for the MC simulation (10^8 photons), cloud thickness h = 300 m and the horizontal pixel size = 12.5 m. The basic cloud element is 2^{10}x12.5 m ≈ 12.8 km long (with no variability in the y direction). The lower curve is optical depth, while the two upper curves are the albedo fields. MC and IPA yield almost equal domain-averaged albedo of ≈0.5, but they show different degrees of smoothness (the thickness of the MC curve reflects the level of its numerical noise). (b) A 1-km zoom of Figure 4a where the MC noise, ≈1% of the albedo, is now visible.

scale-break, submitted to *Journal of Atmospheric Sciences*, 1995) for graphical and physical explanations of these rescaling procedures.)

The fundamental result in Brownian motion is that the mean square displacement is proportional to the corresponding time span. The proportionality constant is the diffusivity of the medium, the product of the particle's average velocity (here set to unity), and the step length l_t. Since the random number ρ is the photon's displacement at escape time t_{esc}, we can write

$$\langle \rho^2 \rangle \sim l_t t_{esc}. \tag{20}$$

Next we estimate the average time t_{esc} which photons spend traveling from x_{in} to x_{out}. Since the photons have a constant speed equal to unity, this time is equal to the distance traveled. Thus, taking into account the rescaled number of scatterings, we have

$$t_{esc} \sim (1-g)N(\tau,g)\, l_t. \tag{21}$$

Substituting (18), (19) and (21) into (20), we have

$$\langle \rho^2 \rangle \sim h^2/(1-g)\tau \quad \textit{albedo case}$$
$$\langle \rho^2 \rangle \sim h^2 \quad \textit{transmittance case} \tag{22}$$

Notice that in case of transmittance the second moment of ρ depends on neither τ nor on g!

To estimate the characteristic size of the spot ⟨ρ⟩ from its second moment ⟨ρ²⟩, we have to make an assumption about the distribution of ρ. If the distribution of ρ is relatively narrow, "short-tailed" according to *Waymire and Gupta*'s [1981] classification, then and only then are we justified in estimating ⟨ρ⟩ from ⟨ρ²⟩$^{1/2}$. This gives us

$$\langle \rho \rangle \approx h[\tau(1-g)]^{-1/2} \quad \textit{albedo case}$$
$$\langle \rho \rangle \approx h \quad \textit{transmittance case.} \tag{23}$$

(We have deliberately used the "approximately equal to" relation here because the numerical data in Figures 6 and 7 support a prefactor of order unity.) Note that, for reflected photons, (23) tells us that ⟨ρ⟩ is roughly equal to the harmonic mean of transport mean free path l_t in (19) and geometrical cloud thickness h. For transmitted photons, however, ⟨ρ⟩ is independent of both τ and g; a simple geometrical explanation of this is given by A. Davis, A. Marshak, R. Cahalan, and W. Wiscombe (Horizontal radiative fluxes in stratocumulus and the Landsat scale-break, submitted to *Journal of Atmospheric Sciences*, 1995).

Our numerical simulations show, on the one hand, that the distribution of ρ is indeed narrow enough to justify (23) and, on the other hand, that relations (22) and (23) are also valid

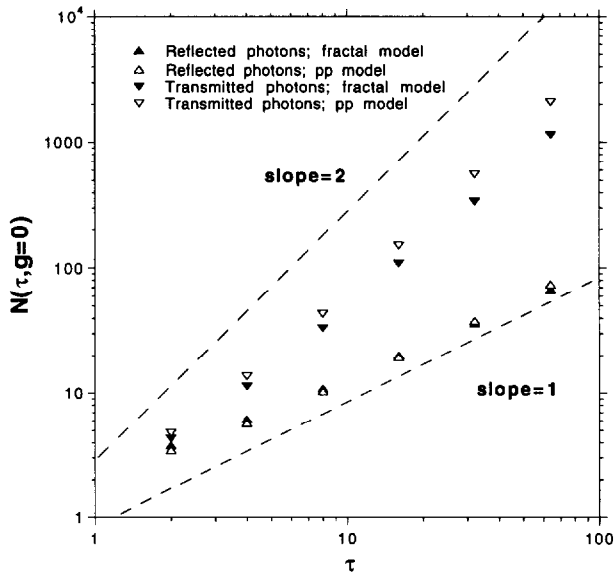

Figure 5. Average number of scatterings versus mean optical depth for homogeneous and fractal models. Diffuse sources uniformly distributed over the upper boundary are used. In the fractal case the horizontal distribution of optical depth is simulated with a bounded cascade model with 10 steps, H = 1/3 and p = 0.25, cloud thickness h = 300 m, and horizontal pixel size 6.25 m. Optical depth τ (⟨τ⟩ in the fractal case) goes from 2 to 64, and scattering is isotropic (g = 0).

for cloud models with stochastically continuous fractal structure. Figure 6 illustrates the first and second moments of ρ for reflected photons and first moments for transmitted photons for both plane-parallel and fractal models (diffusely illuminated and isotropically scattering, as in Figure 5). We see that $\langle\rho\rangle$ for transmitted photons shows a trend toward constancy as τ (or $\langle\tau\rangle$) becomes large, as predicted by the diffusion-based result in (22) and (23). Plotted on double log axes, $\langle\rho^2\rangle$ for reflected photons closely follows the -1 slope for both models, as predicted in (22). The corresponding empirical $\langle\rho\rangle$, not $\langle\rho^2\rangle^{1/2}$, does not follow exactly the $1/\tau^{1/2}$ behavior predicted in (23) but the formula remains good enough to be useful in the parameterization proposed in the following. In summary, we conclude that relations (22) and (23), derived for the homogeneous case, are also valid for bounded cascade models with different prefactors.

Van de Hulst [1980, p. 585] finds that the distribution of photon optical path in homogeneous plane-parallel media can be well approximated by gamma distributions:

$$p(\alpha,\langle x\rangle; x) = \frac{1}{\Gamma(\alpha)(\langle x\rangle/\alpha)^{\alpha}} x^{\alpha-1} \exp[-\alpha x/\langle x\rangle] \quad x > 0$$

$$p(\alpha,\langle x\rangle; x) = 0 \quad x \le 0 \tag{24}$$

where $\Gamma(\cdot)$ is Euler's gamma function, and

$$\alpha = \frac{\langle x\rangle^2}{\mathrm{var}(x)}, \tag{25}$$

with $\mathrm{var}(x) = \langle x^2\rangle - \langle x\rangle^2$. These are typical "short-tailed" distributions. Since ρ, optical path, and orders of scattering are all closely related, this is a useful model for ρ as well. Our numerics confirm that the distribution of ρ is well approximated by (24) for both homogeneous and fractal models. Figures 7a, 7b, and 7c show numerically estimated probability density functions and gamma distributions for reflected and transmitted photons; a homogeneous medium with $\tau = 16$ and isotropic scattering (Figure 7a) is illustrated along with a fractal model with $\langle\tau\rangle = 16$ and $g = 0.00$ (Figure 7b) and $g = 0.85$ (Figure 7c). Notice that for reflected photons, α is smaller than 1, while for transmitted photons, α is significantly larger than 1. This means that many of the photons exit the cloud top very near the entry point, leading to a weak (integrable) singularity at $\rho = 0$ in the function describing the spot's shape. In sharp contrast, the transmitted spot's intensity is maximum not directly below the entry point but about 200–300 m away, a distance close to the geometrical thickness $h = 300$ m.

6. "Nonlocal" Independent Pixel Approximation

6.1. Spot Shape as a Smoothing Kernel

On the one hand, MC is time consuming but accurate; on the other hand, the IPA is fast and in certain instances yields a good approximation; for example, IPA and MC domain-averaged albedos are close for Sc cloud models cf. (Figures 3 and 4 and *Cahalan et al.* [1994b] for a systematic study of IPA-to-MC differences.) There is nothing between these two extremes. How can the IPA be improved (made to agree better with MC results) without sacrificing too much of its computational advantage in speed?

The above results allow us to improve the IPA by incorporating the smoothing effects of horizontal interpixel fluxes. As a first approximation we can consider the convolution of $R_{IP}(x)$ with $0.5\, p(\alpha,\langle\rho\rangle; |x|)$, i.e.,

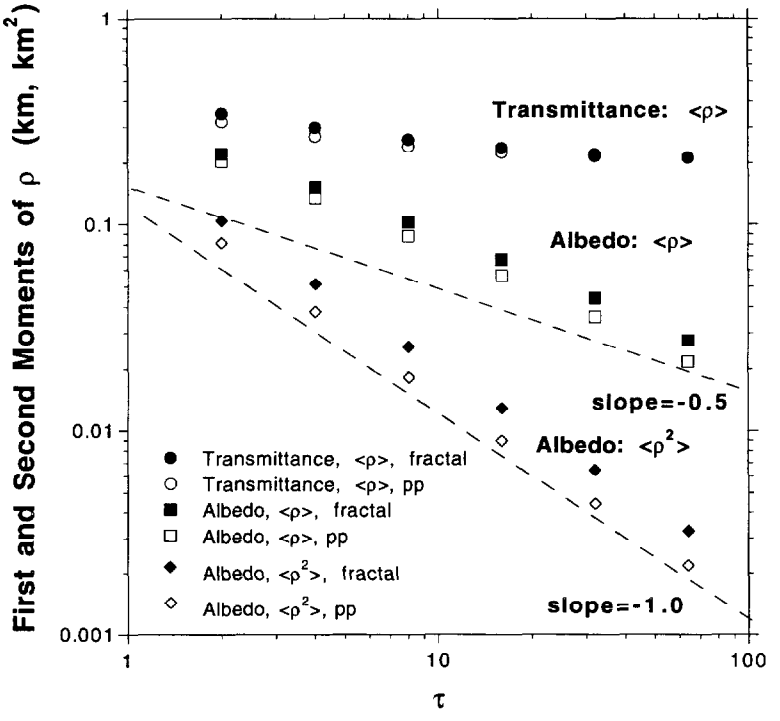

Figure 6. First and second moments of ρ, the horizontal distance between the photon's entry and exit points, versus mean optical depth. The fractal model of optical depth, range of τ and $\langle\tau\rangle$, the sources, and scattering properties are as in Figure 5. Only 4 million photons are need to cumulate the MC statistics for this, the previous, and the following figures.

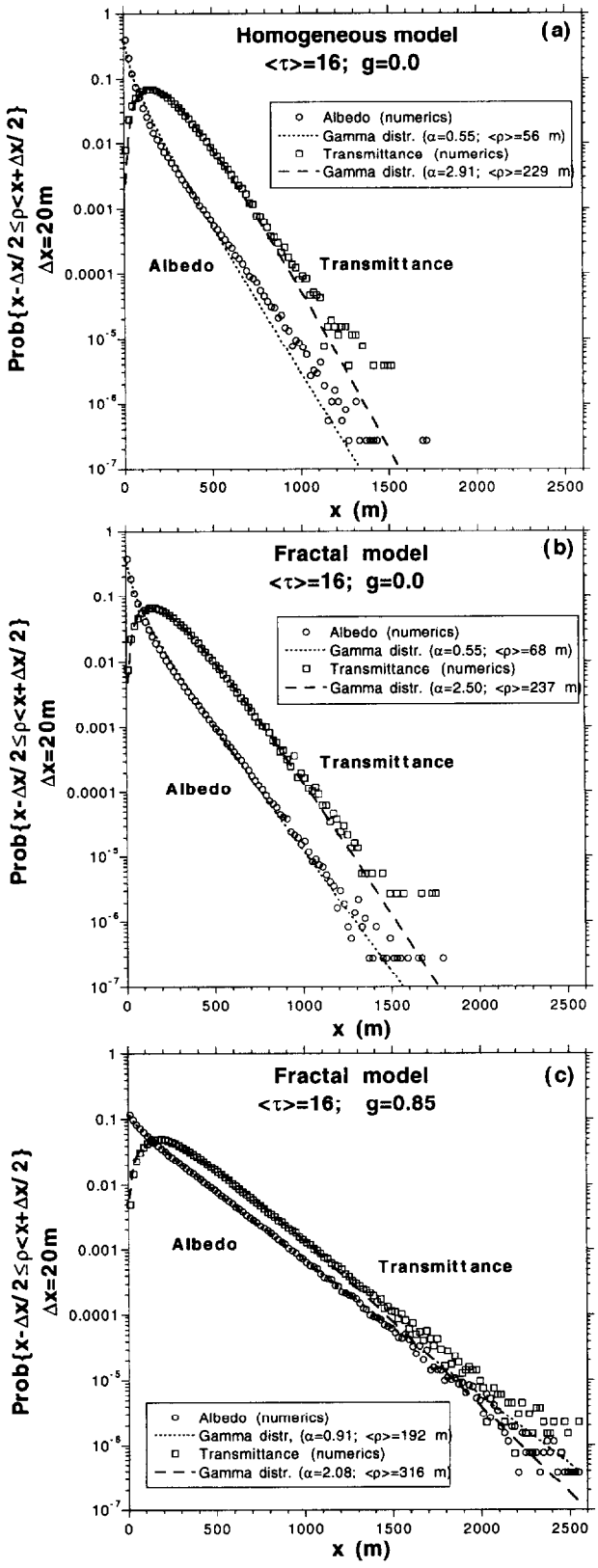

Figure 7. Probability density function of ρ. (a) Homogeneous case with $\tau = 16$ and isotropic scattering. (b) Fractal optical depth model used in Figure 5 with $\langle\tau\rangle = 16$ and isotropic scattering. (c) Same as Figure 7b, but scattering is anisotropic ($g = 0.85$). In all cases, numerical results and gamma distributions (24) are presented for both reflected and transmitted photons. Numerically calculated values of $\langle\rho\rangle$ and $\langle\rho^2\rangle$ are used to parameterize tne model distribution.

$$R_{\mathrm{NIP}}(x) = \frac{1}{2}\int_{-\infty}^{\infty} R_{\mathrm{IP}}(x')\, p(\alpha,\langle\rho\rangle;\, |x-x'|)\, dx' \qquad (26)$$

where $\langle\rho\rangle$ is defined in (23) and α can be set a priori. The subscript NIP stands for "nonlocal independent pixels." To approximate the MC albedo results in Figure 4a ($\langle\tau\rangle = 13$, $h = 0.3$ km, $g = 0.85$, $\theta_0 = 22.5°$) using NIP, we take $p(\alpha,\langle\rho\rangle;\, |x|)$ with $\alpha = 1/2$ for simplicity and $\langle\rho\rangle = 0.3\mathrm{km}/[(1-0.85)\times 13]^{1/2} \approx 0.215$ km from (23). In Figures 8a and 8b we plotted the three albedo fields, R_{IP}, R_{MC} and R_{NIP}, along with $R_{\mathrm{MC}}-R_{\mathrm{NIP}}$.

The convolution product in (26) is best done in Fourier space:

$$\tilde{R}_{\mathrm{NIP}}(k) = \tilde{R}_{\mathrm{IP}}(k)\tilde{p}(\alpha,\langle\rho\rangle;\, k), \qquad (27)$$

with [*Gradshteyn and Ryzhik*, 1980]

$$\tilde{p}(\alpha,\langle\rho\rangle;\, k) = \int_0^{\infty} p(\alpha,\langle\rho\rangle;\, x)\, \cos(xk)\, dx = \frac{\cos[\alpha \tan^{-1}(\langle\rho\rangle k/\alpha)]}{[1 + (\langle\rho\rangle k/\alpha)^2]^{\alpha/2}}. \qquad (28)$$

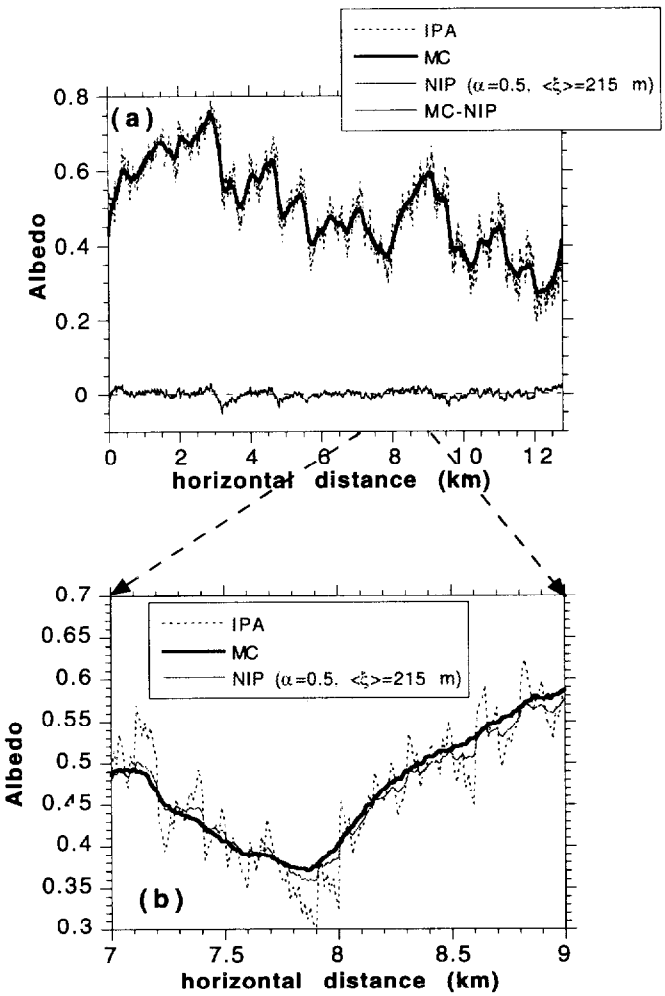

Figure 8. Nonlocal independent pixel approximation. (a) Three albedo fields calculated by the IPA, MC, and the improved "nonlocal" IPA in (26) are presented along with the residuals between the last two. The first two fields are the same as in Figure 4a. (b) Zoom into Figure 8a to show the differences between MC and the new nonlocal IPA scheme.

This convolution does not affect the domain average in any way, since $\tilde{p}(\alpha,\langle\rho\rangle; 0) = 1$; it only dampens the small-scale fluctuations of $R_{IP}(x)$. The energy spectrum of the NIP field is given by

$$E_{R_{NIP}}(k) = |\tilde{R}_{IP}(k)|^2 \tilde{p}(\alpha,\langle\rho\rangle; k)^2 = E_{R_{IP}}(k)\frac{\cos^2[\alpha \tan^{-1}(\langle\rho\rangle k/\alpha)]}{[1 + (\langle\rho\rangle k/\alpha)^2]^\alpha}, \quad (29)$$

where $E_{R_{IP}}(k) \sim k^{-5/3}$. Special cases of interest are $\alpha = 1$, where (24) becomes an exponential distribution:

$$E_{R_{NIP}}(k) = E_{R_{IP}}(k)\tilde{p}(1,\langle\rho\rangle; k)^2 \sim \frac{k^{-5/3}}{[1 + (\langle\rho\rangle k)^2]^2} \sim k^{-17/3} \text{ as } k \to \infty; \quad (30)$$

and $\alpha = 1/2$:

$$E_{R_{NIP}}(k) = E_{R_{IP}}(k)\tilde{p}(\tfrac{1}{2},\langle\rho\rangle; k)^2 \sim k^{-5/3}\left[\frac{1}{\sqrt{1 + (2\langle\rho\rangle k)^2}} + \frac{1}{1 + (2\langle\rho\rangle k)^2}\right] \sim k^{-8/3} \text{ as } k \to \infty. \quad (31)$$

In general, a little algebra shows that the small scale (large k) behavior is $E_{R_{NIP}}(k) \sim k^{-(5/3+\Delta\beta)}$ with

$$\Delta\beta = 2\alpha \quad \alpha \neq 1, 3, 5, \ldots, \text{ (asymptotic approach from above)}$$
$$\Delta\beta = 2(\alpha+1) \quad \text{otherwise (asymptotic approach from below).} \quad (32)$$

Figure 9 illustrates $E_{R_{NIP}}(k)$ for $\alpha = 0$, 1/2, 3/4, and 1.

We see from (29) that for small wavenumbers k (large scales), both R_{IP} and R_{NIP} have the same spectrum which follows a $k^{-5/3}$ power law, while for large k (small scales) the behavior is quite different. Being scale-invariant, R_{IP} has a $k^{-5/3}$ spectrum for all scales, while R_{NIP} exhibits much smoother behavior for small scales (its spectrum steepens). For sufficiently large α the nonlocal IPA albedo field becomes differentiable ($\beta \geq 3$). As a result, we have two distinct power law regimes for large and small scales; the characteristic ("radiative smoothing") scale which separates these two regimes is given by $\langle\rho\rangle$.

6.2. Application to the Scale Break in Landsat Radiation Fields

Cahalan and Snider [1989] studied the scaling properties of Landsat cloud scenes for marine Sc. They found that for scales larger than $\eta \approx 200$ m the radiation energy spectrum follows the one of cloud liquid water (roughly a $k^{-5/3}$ power law), while at smaller scales it exhibits a much smoother behavior, with spectral exponent β in excess of 3. Hence they reported a scale break in the radiation energy spectrum and the existence of a characteristic scale separating two distinct power law regimes. The mechanism of this scale break is now clear: horizontal radiative transport smoothes out the small-scale features of the underlying extinction field.

Figure 10 shows a one-dimensional energy spectrum $E(k)$ for a Landsat scene of marine Sc captured on June 30, 1987; this is different from Cahalan and Snider's July 7 data, although it originates from the same First International Satellite Cloud Climatological Project Regional Experiment database. Furthermore, Cahalan and Snider selected a few lines to produce their spectrum; here we systematically average $E(k)$ over 4096 (120 km long) lines of 4096 (30 m wide) pixels. As a result the noise level is very low. For scales larger than $\eta \approx 0.2$ km, $E(k)$ follows a $k^{-1.8}$ law, close to the $k^{-5/3}$ scaling observed for cloud liquid water; at smaller scales, $E(k)$ goes as

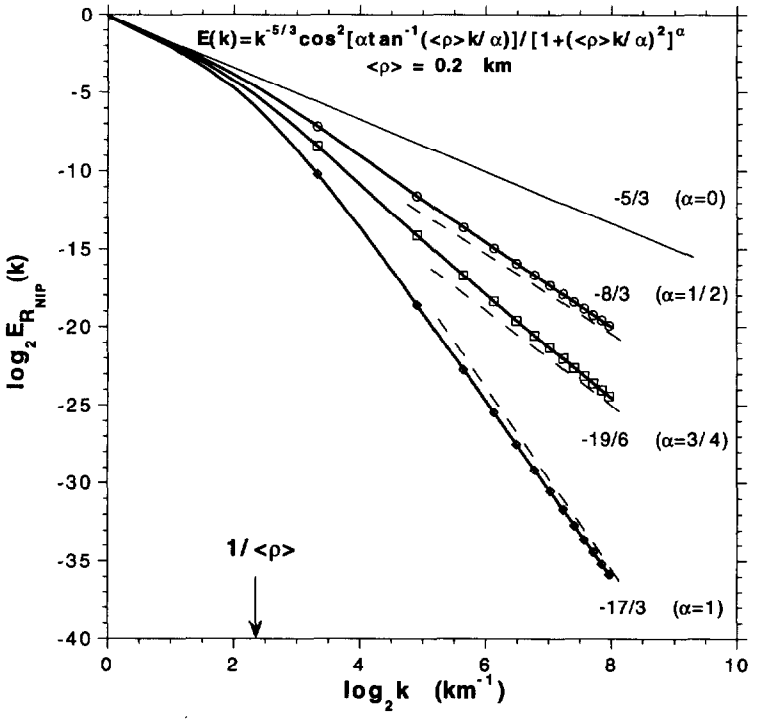

Figure 9. Energy spectra for nonlocal IPA fields of scale-invariant cloud models. Equation (29) is plotted for an IP reflectivity field that scales in $k^{-5/3}$ for $r = 1/k$ down to ≈4 m (only $r \geq 1$ km is illustrated); $\langle\rho\rangle$ is held constant at 200 m, and $\alpha = 0$, 1/2, 3/4, 1.

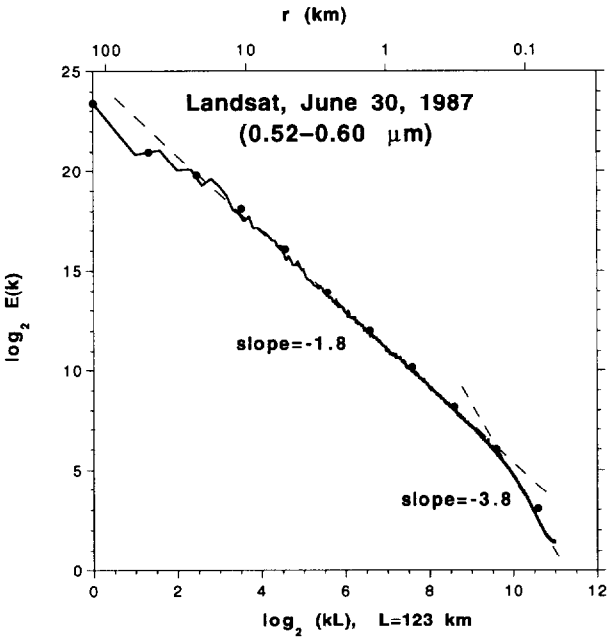

Figure 10. Energy spectrum of a Landsat radiance field. A log-log plot of $E(k)$ versus k for a Landsat Thematic Mapper 4096 x 4096 subimage of a marine Sc deck in channel 2 (0.52 – 0.60 μm) captured on June 30, 1987 during FIRE. Pixels are 30x30 m^2 (note the distance scale on the top axis). The image was Fourier transformed line by line in one direction, and the resulting $E(k)$ values were averaged the over the other direction. Statistical noise is thus reduced to the point where the small "whitening" effect of digitization noise appears at the very smallest scales (largest k values), at the level of ±1 bit in the 8-bit data. The solid circles correspond to the octave-binning representation used in Figure 2.

$k^{-3.8}$. Recall that for typical marine Sc values (τ = 13, g = 0.85), equation (23) yields 215 m for $\langle\rho\rangle$, very close to η. At the very smallest scales the influence of digitization noise (±1 bit out of the 8-bit Landsat data) can just barely be seen.

In order to explain the mechanism of the Landsat scale break we investigated numerically the dependence of the scale break location η on h, τ, g, on the variability parameters of the fractal model (e.g., p and H in (10)), and on the choice of fractal model. We found that the characteristic scale behaves exactly like the spot size resulting from localized beam illumination, as determined in section 5.2 in the frame of diffusion theory; we also found that the fractal variability parameters and model choice play a small role in comparison with h, τ, and g. In particular, both the spot size and the scale break are proportional to the square root of the product of transport mean free path l_t in equation (19) and geometrical cloud thickness h, not to l_t itself, as was first thought [*Cahalan and Snider*, 1989]. More details will be presented in a forthcoming publication by A. Davis, A. Marshak, R. Cahalan, and W. Wiscombe (Horizontal radiative fluxes in stratocumulus and the Landsat scale-break, submitted to *Journal of Atmospheric Sciences*, 1995).

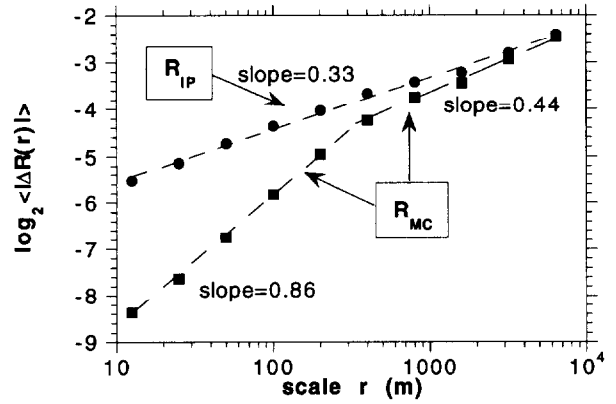

Figure 11. IPA/MC comparison with first-order structure functions. Scaling of the q = 1 structure functions for the IPA and MC albedo fields from Figure 4a. For the latter case the scale break is around 200–400 m. The slopes define the mean Hölder exponents $H_1 = \zeta(1)$.

7. Radiative Smoothing and Remote Sensing of Cloud Optical Depth Fields

7.1. Scaling Properties

To study the smoothness properties of the cloud reflectivity field, we use the structure function approach defined in (5). Figure 11a shows the first-order structure function for the IPA and MC albedo fields in Figure 4a. Being more sensitive to the variability at any scale, the structure function exponent shows a difference even for large scales (0.33 versus 0.44). This difference, however, becomes much larger for small scales (0.33 versus 0.86); the scale break is clearly seen at 200–400 m, as observed in Landsat images. This quantifies the smoothness of the MC albedo field seen in Figure 4 and we note that the Hölder exponent H_1 = 0.86 is not far from the differentiability limit H_1 = 1.0 (the difference is possibly due to a combination of numerical noise and finite size effects).

We note that *Marshak et al.* [1995] compared the smoothness properties of IPA and MC albedos differently. They characterized radiative smoothing by showing that the "effective" spectral exponent for MC—defined numerically, all scales combined—was larger than the "original" value obtained for optical depth (or IPA). In contrast, we describe how much the scaling regime where the IPA is validated by MC results is reduced from below. Marshak et al.'s procedure was justified on operational grounds because they considered a relatively small range of scales; their cloud model was a single two-dimensional bounded cascade with only seven steps, yielding a 128x128 horizontal grid, and they averaged their spectra over 64x64 boxes.

7.2. From Albedo to Nadir Radiance

Albedo is more difficult to measure than nadir radiance, for reasons related both to the field of view and to instrument design. Our code was therefore modified to estimate local radiances in vertical directions with accuracies usually obtained only for fluxes (see Appendix A). However, not much difference was found in the scaling properties of nadir radiance and albedo. Figure 12 shows two structure functions (q=2 and q=4) for albedo and nadir radiance calculated by MC. Again both structure functions show the scale break.

Figure 13 shows the structure function exponents $\zeta(q)$ plotted versus q for scales either smaller or larger than 300 m for MC nadir radiance. At small scales the structure functions of MC radiance do not show much multifractality (deviation of $\zeta(q)$ from a straight line). In this case the Hölder exponent,

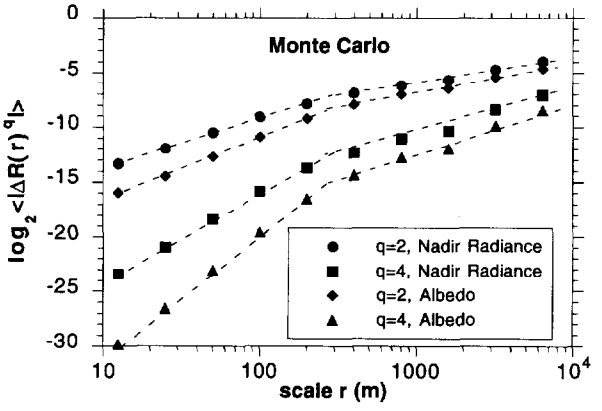

Figure 12. Radiance/albedo comparison with qth-order structure function analysis. Scaling of the $q = 2$ and $q = 4$ structure functions for MC nadir radiance and albedo fields. (The former is computed with high accuracy by using the technique described in Appendix A; the latter is obtained from Figure 4a). The scale break is again clearly seen around 200–400 m. In both regimes the albedo slope is slightly larger than its counterpart for nadir radiance.

$H_1 = \zeta(1)$ (highlighted in Figure 12), defines $\zeta(q)$ accurately. Notice that $H_1 = 0.86$ for albedo (from Figure 11) and $H_1 = 0.71$ for nadir radiance (from Figure 13); because of the averaging over azimuthal and polar angles, the albedo field is smoother than nadir radiance; thus its Hölder exponent, an indicator of smoothness, is expected to be larger.

7.3. Assessment of IPA Retrievals with Multifractal Statistics

Results for IPA radiances, obtained from DISORT and representative of all scales, are also indicated in Figure 13. The IPA exponents are very close to those of the bounded cascade model for liquid water (see equation (13)). This means that at the larger scales where it is useful the IPA can be applied to remotely sensed data to retrieve both one-point statistical properties of liquid water path and its two-point correlations but only for low-order moments (such as means and variances). This follows from the fact that in retrieval mode the IPA is applied to the real world counterparts of our large-scale MC fields, which have the same $\zeta(q)$ as optical depth only up to $q \approx 2$. Since higher q values emphasize larger jumps in the field of interest [e.g., *Davis et al.*, 1994], this means the largest jumps in optical thickness are more radiatively smoothed than their average counterparts.

To estimate the effect of radiative smoothing on the optical depth retrieval, A. Davis, A. Marshak, R. Cahalan, and W. Wiscombe (Horizontal radiative fluxes in stratocumulus and the Landsat scale-break, submitted to *Journal of Atmospheric Sciences*, 1995) use a simple plane-parallel retrieval algorithm and compute the average relative retrieval error as a function of instrumental resolution. They found about 8% error for smallest resolution (12.5-m pixels); as the scale increases, the error sharply decreases to ≈4% around the radiative smoothing scale η (200-400 m) and eventually reaches a minimum of ≈2% around 1 km scale. After this it increases, reaching its maximum of 11% for the domain average, which is related to *Cahalan et al.*'s [1994b] "plane-parallel bias." Thus we see that from the standpoints of this simple statistic as well as the multifractal statistics used in this paper, one must degrade the resolution of the measured radiance field, at least to the radiative smoothing scales η, in order to get rid of the radiative smoothing and obtain reliable optical depth retrievals. If this is done, A. Davis, A. Marshak, R. Cahalan, and W. Wiscombe (Horizontal radiative fluxes in stratocumulus and the Landsat scale-break, submitted to *Journal of Atmospheric Sciences*, 1995) show that, given the inferred optical depth field at resolution η, errors as small as 0.3% are obtained for the domain average; this small residual error is commensurate with *Cahalan et al.*'s [1994b] "IPA bias."

Our simulations suggest that the above shortcomings of current IPA retrieval methods can be overcome by "deconvolving" small-scale radiometric data with a "roughening" kernel prior to applying the inverse IPA scheme. More realistic (rougher) optical depth fields will be obtained but instrumental noise (cf. Figure 10) will also be amplified. Further discussion of this important application is outside the scope of this paper.

8. Summary and Conclusions

Motivated by in situ and ground-based (microwave) probings of real clouds, the horizontal distribution of cloud optical depth was modeled as a scale-invariant multifractal cascade. Multiplicative weights in the cascade model (7) converge to unity as the cascade proceeds (10). As a result, we obtain a scale-invariant bounded cascade model with a wavenumber spectrum $\sim k^{-\beta}$, with $\beta > 1$. In particular, $\beta \approx 5/3$ is typical of that observed in marine Sc.

The IPA computes the radiation properties of each pixel by treating it as a homogeneous plane-parallel layer, ignoring net horizontal transport. It is routinely used in current remote

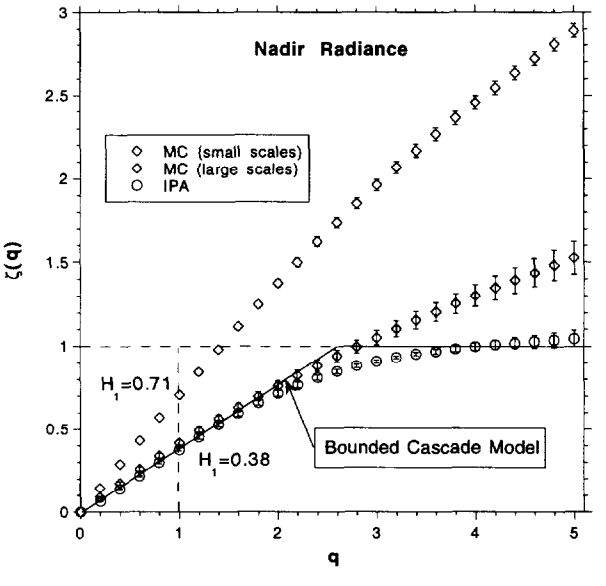

Figure 13. Structure function exponents $\zeta(q)$ for nadir radiance. The IPA (DISORT) results are representative of all scales and closely follow the theoretical values for the optical depth field in (13). For MC, both small-scale (≤ 300 m) and large-scale regimes are indicated; only the large-scale results are useful as estimates for the statistics of the optical depth field and only for the low-order moments at that. The mean Hölder exponents $H_1 = \zeta(1)$ are highlighted, being direct measures of the smoothnesses of the corresponding fields.

sensing applications to infer inherent cloud properties from measured radiance fields. However, clear differences emerge when IPA albedos and nadir radiances for realistic multifractal clouds are compared with accurate Monte Carlo radiative transfer calculations. Spectral analysis shows that in the MC case there is a well-defined characteristic scale η we call the "radiative smoothing scale" that separates two physically distinct regimes:

1. For scales larger than η, IPA and MC fields have the same power law energy spectrum. Moreover, these radiation fields fluctuate in phase with the underlying optical depth field. Thus, at these scales, the optical depth field can be retrieved from the radiation fields by using plane-parallel theory, i.e., an IPA hypothesis. However, the statistical properties of the inferred optical depth field are realistic only for low-order moments (Figure 13).

2. For scales smaller than η, MC fields have a spectral exponent in excess of 3, whereas their IPA counterparts continue to scale almost like the optical depth field. This small-scale regime is dominated radiatively by horizontal interpixel transport processes. Consequently, real albedo/radiance fields are much smoother than the IPA indicates, and IPA-based retrievals of optical depth will vastly underestimate liquid water variability at these scales.

To strengthen our point, we recall that Landsat radiances exhibit a break in scaling properties at 200–500 m, precisely where we predict it to occur.

To complement spectral analysis, we used structure function analysis (5) to study the scale break in physical rather than Fourier space. The scaling exponent of the first-order structure function H_1, also called Hölder exponent (see equations (2) and (3)), characterizes the smoothness properties of a stochastic process. We found that H_1 is equal to 0.3–0.4 for both the horizontal distribution of the optical depth and the largest scales of the albedo and nadir radiance fields. However, it changes to 0.8–0.9 for the smallest scales of the radiation fields emerging from our fractal scale-invariant cloud model. (Differentiable functions are characterized by $H_1 = 1$.)

We argue that η is determined entirely by the characteristic size of the spot resulting from localized beam illumination. First, we set up a boundary value problem to determine the scaling properties of the spot size; its solution gives us the average optical path in a homogeneous plane-parallel medium in the diffusion approximation. Then Brownian motion theory is invoked and to the spot size as a function of the three main parameters of the radiative transfer problem: the optical thickness τ, the cloud's vertical extent h, and the asymmetry factor g. We find that for reflected photons the spot size is given to a good approximation by the harmonic mean of the geometrical cloud thickness h and the transport mean free path, $h/[(1-g)\tau]$. The size of the spot in transmittance is simply proportional to h, independently of τ and g. These spot size results are generalized to a class of stochastically continuous fractal cloud models based on bounded cascades by using numerical Monte Carlo calculations. Finally, we show that the distributions of the horizontal distance between photon penetration and escape points are well approximated by gamma distributions (24).

If the shape of the spot is known, then the effect of the horizontal photon transport can be estimated. More precisely, IPA fields can be corrected by convolution with the probability density function describing the spot. The improved "nonlocal" IPA will generate smoother fields at small scales and leave large-scale properties unchanged. Conversely, radiation fields measured at resolutions finer than the smoothing scale (e.g., Landsat) should be correspondingly "roughened" before applying IPA-based retrieval schemes down to the smallest observable scales.

Appendix A: Monte Carlo Techniques

We describe here the lesser-known Monte Carlo tricks used in sections 4–5 of the paper.

A.1. Maximum Cross-Section Method

The "Maximum Cross-Section Method" [*Marchuk et al.*, 1980] involves transforming the transfer equation from

$$\Omega\cdot\nabla I(r;\Omega) + \sigma(r)I(r;\Omega) = \varpi_0\,\sigma(r)\int_{4\pi} P(\Omega\cdot\Omega')I(r;\Omega')\,d\Omega' \quad \text{(A1)}$$

where ϖ_0 is the single-scattering albedo and $P(\Omega\cdot\Omega')$ is the phase function, to

$$\Omega\cdot\nabla I(r;\Omega) + \sigma_{max}I(r;\Omega) = \sigma_{max}\int_{4\pi}\left[\frac{\sigma(r)}{\sigma_{max}}\varpi_0 P(\Omega\cdot\Omega') + \left(1-\frac{\sigma(r)}{\sigma_{max}}\right)\delta(\Omega-\Omega')\right] I(r;\Omega')\,d\Omega' \quad \text{(A2a)}$$

where $\sigma_{max} = \max_r\{\sigma(r)\}$ is the maximal extinction. Equation (A2a) can be interpreted as the transport equation with constant extinction and a modified phase function equal to

$$\begin{cases} \varpi_0 P(\Omega\cdot\Omega') & \text{with probability } \sigma(r)/\sigma_{max}, \\ & \text{(this is a "physical" scattering)} \\ \delta(\Omega-\Omega') & \text{otherwise (this is a "mathematical" one).} \end{cases} \quad \text{(A2b)}$$

The former occurrence is the usual case; the latter is not unlike that in a δ-Eddington parameterization (but in a position dependent manner).

In this method the photon jumps immediately to its next (physical or mathematical) scattering point instead of accumulating optical depth cell by cell and interpolating within the last one. This makes the computer time almost insensitive to (1) whether we use one-dimensional, two-dimensional, or three-dimensional geometry; (2) the variability of $\sigma(r)$, except for very large σ_{max} (hence very small steps); (3) the number of cells.

All three of these factors substantially slow the execution of standard MC codes for inhomogeneous media. In fully vectorized mode [*Cahalan et al.*, 1994b] the above technique is even more economical: on a Cray YMP, rates in excess of a million photons per CPU-second have been achieved.

A.2. Nadir and Zenith Radiances in a Forward Monte Carlo Scheme

Simultaneously with exiting fluxes, the usual output with forward MC, we can compute nadir and zenith radiances; this computation is usually done with a backward MC approach. Vertical radiances I_j for each cell S_j on a one- or two-dimensional horizontal grid are estimated by the flux of radiant energy across (1) the upper boundary of S_j (at $z = h$) in the zenith direction (Ω_+), described as "nadir radiance" in the main text, which takes the observer's standpoint, or (2) the lower boundary of S_j (at $z = 0$) in the nadir direction (Ω_-) where h is the cloud's vertical thickness. In other words,

$$I_j(\Omega_\pm) = \int_{S_j} I(\boldsymbol{r}(x);\Omega_\pm)\,dx = E[\xi_j(\Omega_\pm)], \tag{A3}$$

where $E[\cdot]$ denotes an average over all histories. The random value $\xi_j(\Omega_\pm)$ is the contribution to the grid point S_j i n direction $\Omega_\pm$ from all orders of (physical) scattering:

$$\xi_j(\Omega_+) = \sum_{k=1}^{N} \varpi_0{}^k P(\Omega_k\cdot\Omega_\pm)\,\chi_j(k)\exp[-\sigma_j(h-z_k)] \quad \text{zenith} \tag{A4a}$$

$$\xi_j(\Omega_-) = \sum_{k=1}^{N} \varpi_0{}^k P(\Omega_k\cdot\Omega_\pm)\,\chi_j(k)\exp[-\sigma_j z_k] \quad \text{nadir}$$

where N is the (random) last scattering order of the photon trajectory under consideration, σ_j is the extinction of the grid point S_j, $\boldsymbol{x}_k = (x_k, y_k, z_k)^T$ are the coordinates of the point at which the photon suffered its kth scattering, and Ω_k is its direction of propagation before this scattering event.

Finally, $\chi_j(k)$ indicates whether the photon was in cell S_j or not at its kth scattering:

$$\chi_j(k) = 1 \quad x_k y_k \in S_j$$
$$\chi_j(k) = 0 \quad \text{otherwise.} \tag{A4b}$$

Formulae (A4a) can be evaluated at a relatively small extra computational cost in a forward MC scheme; however, vectorization is inhibited, at least with Cray compilers, due to the contingency in (A4b).

Appendix B: Average Number of Scatterings Suffered by Reflected and Transmitted Photons

In this appendix we show that in the diffusion approximation for conservative scattering, the average number of scatterings is proportional to optical thickness τ for albedo and to $(1-g)\tau^2$ for transmittance where, g is the phase function's asymmetry parameter. We first consider the simplest possible time-dependent boundary-value problem, a plane-parallel medium of geometrical size h with conservative scattering ($\varpi_0 = 1$):

$$\begin{cases} \dfrac{\partial J}{\partial t} - D\,\dfrac{\partial^2 J}{\partial^2 z} = \sigma S(t,z),\ 0 \le t \le \infty,\ 0 \le z \le h \\ J(0,z) = 0,\ \left[J - \chi\dfrac{dJ}{dz}\right]_{z=0} = \left[J + \chi\dfrac{dJ}{dz}\right]_{z=h} = 0 \end{cases}, \tag{B1}$$

where $S(t,z)$ is the source term, χ is the extrapolation length, and $D = [3\sigma(1-g)]^{-1}$ is the diffusion coefficient. We assume that the source is well localized in time and that the average time of emission is zero, i.e.,

$$\int_0^\infty t \int_0^h S(t,z)dz\,dt \Big/ \int_0^\infty \int_0^h S(t,z)dz\,dt = 0; \tag{B2}$$

on physical grounds, this implies $\lim_{t\to\infty} J(t,z) = 0$. Given the solution $J(t,z)$ of the boundary value problem (B1), the characteristic time t_{esc} for photons to be transported from their source to a boundary h is the ratio of

$$\int_0^\infty t\,\left[\frac{\partial J}{\partial z}(t,z_0) - \frac{\partial J}{\partial z}(t,0)\right] dt = \int_0^\infty t \int_0^h \frac{\partial^2 J}{\partial^2 z}(t,z)dz\,dt \tag{B3}$$

to the same expression but without the factor of t. The two terms on the left-hand side of (B3) are proportional to the exiting fluxes at $z=z_0$ and $z_0=0$, respectively (Fick's law). Taking into account equation (B1) and integrating by parts the left-hand side of (B3), we obtain the average optical path

$$\sigma t_{esc} = \frac{\int_0^\infty \int_0^h J(t,z)dz\,dt}{\int_0^\infty \int_0^h S(t,z)dz\,dt}. \tag{B4}$$

(Equality (B4) is in fact valid for the more general case of three-dimensional homogeneous media without the diffusion approximation; equation (B1) then will be the equation of energy conservation, and (B3) will read as Ostrogradski's formula.)

Next we consider a steady state boundary value problem [$\partial J/\partial t \equiv 0$ and $S(t,z) \equiv S(z)$]. It is easy to verify that the Green's function $G(z,z^*)$ for this problem, $J(z)$ with $S(z) = \delta(z-z^*)$, is

$$G(z,z^*) = \frac{\sigma}{D(h+2\chi)}(z+\chi)(\chi-z^*+h) \quad z < z^*$$
$$G(z,z^*) = \frac{\sigma}{D(h+2\chi)}(z^*+\chi)(\chi-z+h) \quad z > z^* \qquad 0 \le z^* \le h. \tag{B5}$$

Dropping the time integrations in (B4), we obtain

$$\sigma t_{esc} \sim \frac{\int_0^h G(z,z^*)dz}{\int_0^h S(z)dz} = \frac{\sigma h}{2D}\chi + \frac{\sigma z^*}{2D}(h-z^*) \tag{B6}$$

for the average optical path. This is roughly equal to the average number of scatterings $N(h)$, in optically thick media ($\tau = \sigma h \gg 1$), and hence

$$N(h) \approx \frac{\sigma}{2D}[\,\chi + A(1-A)h\,]h \quad 0 \le A = \frac{z^*}{h} \le 1. \tag{B7}$$

We see that if the source is located on a boundary [$z^* = 0$ ($A = 0$) or $z^* = h$ ($A = 1$)], then $N(h)$ is proportional to h (this is characteristic of reflection); otherwise, $N(h) \sim h^2$ (this is characteristic of transmittance). Recalling that $D = 1/3[(1-g)\sigma]^{-1}$ and $\chi = 2D$ in Eddington's approximation, we find from equation (B7)

$$N(g,\tau) = \tau \quad \textit{for reflected photons}$$
$$N(g,\tau) = (1-g)\tau^2 \quad \textit{for "transmitted" photons.} \tag{B8}$$

Consequently, reflected photons (contributing to albedo) are scattered typically τ times, while transmitted photons are scattered τ^2 times in the diffusion regime ($\tau \gg 1$). *Ivanov and Gutshabash* [1974] derived the results in (B8), using an asymptotic expansion of the solution of the exact time-dependent radiative transfer equation, rather than its diffusion counterpart —equivalently, its first-order spherical harmonic truncation. A result similar to (B8) also can be found in *Van de Hulst*'s [1980] monograph *"Multiple Light Scattering"* (vol. II, p. 590). He shows that in case of conservative scattering, the ratio between the mean photon optical path and τ tends to $\mu+\mu_0$ as $\tau\to\infty$. (Here μ and μ_0 are, as usual, the cosines of the reflected and incident beams.)

Acknowledgments. This work was supported by the Environmental Sciences Division of U.S. Department of Energy (under grant DE-A105-90ER61069 to NASA's Goddard Space Flight Center) as part of the Atmospheric Radiation Measurement (ARM) program. We thank H. Barker, A. Ioltukhovski, P. Gabriel, S. Gollmer, Y. Knyazikhin, S. Platnik, W. Ridgway, L. Titarchuk, G. Titov, S.-C. Tsay, and T. Viik for helpful discussions.

References

Barker, H. W., and D. Liu, Inferring optical depth of broken cumulus cloud from Landsat data, *J. Clim.*, in press, 1995.

Cahalan, R. F., Overview of fractal clouds, in *Advances in Remote Sensing Retrieval Methods*, pp. 371–388, A. Deepak, Hampton, Va., 1989.

Cahalan, R. F., Bounded cascade clouds: Albedo and effective thickness, *Nonlinear Proc. in Geophys.*, *1*, 156–167, 1994.

Cahalan, R. F., and J. B. Snider, Marine stratocumulus structure, *Remote Sens. Environ.*, *28*, 95–107, 1989.

Cahalan, R. F., W. Ridgway, W. J. Wiscombe, T. L. Bell, and J. B. Snider, The albedo of fractal stratocumulus clouds, *J. Atmos. Sci.*, *51*, 2434–2455, 1994a.

Cahalan, R. F., W. Ridgway, W. J. Wiscombe, S. Gollmer, and Harshvardan, Independent pixel and Monte Carlo estimates of stratocumulus albedo, *J. Atmos. Sci.*, *51*, 3776–3790, 1994b.

Case, K. M., and P. F. Zweifel, *Linear Transport Theory*, Addison-Wesley, Reading, Mass., 1967.

Davis, A., A. Marshak, W. Wiscombe, and R. Cahalan, Multifractal characterizations of nonstationarity and intermittency in geophysical fields, observed, retrieved or simulated, *J. Geophys. Res.*, *99*, 8055–8072, 1994.

Frisch, U., From global scaling, à la Kolmogorov, to local multifractal in fully developed turbulence, *Proc. R. Soc. London A*, *434*, 89-99, 1991.

Gradshteyn, I. S., and I. M. Ryzhik, *Tables of Integrals, Series, and Products*, Academic, San Diego, Calif., 1980.

Harshvardan, B. A. Wielicki, and K. M. Ginger, The interpretation of remotely sensed cloud properties from a model parameterization perspective, *J. Clim.*, *7*, 1987–1998, 1994.

Henyey, L. C., and J. L. Greenstein, Diffuse radiation in the galaxy. *Astrophys. J.*, *93*, 70–83, 1941.

Ivanov V. V., and S. D. Gutshabash, Propagation of brightness wave in an optically thick atmosphere, *Izv. Akad. Nauk SSSR Fiz. Atmos. i Okeana*, *10*, 851–863, 1974.

Jensen, J. L. W. V., Sur les fonctions convexes et les inégalités entre les valeurs moyennes, *Acta Math.*, *30*, 789–806, 1906.

Lenoble, J., *Radiative Transfer in Scattering and Absorbing Atmospheres: Standard Computational Procedures*, 300 pp., A. Deepak, Hampton,1985.

Li, J., D. J. Geldart, and P. Chylek, Solar radiative transfer in clouds with vertical internal inhomogeneity, *J. Atmos. Sci.*, *51*, 2542–2552, 1994.

Lovejoy S., D. Schertzer, P. Silas, Y. Tessier, and D. Lavallee, The unified scaling model of atmospheric dynamics and systematic analysis of scale invariance in cloud radiances, *Ann. Geophys.*, *11*, 119–127, 1993.

Mandelbrot, B. B. , *Fractals: Form, Chance, and Dimension*, 365 pp., W. H. Freeman, New York, 1977.

Marchuk, G., G. Mikhailov, M. Nazaraliev, R. Darbinjan, B. Kargin, and B. Elepov, *The Monte Carlo Methods in Atmospheric Optics*, 208 pp., Springer-Verlag, New York, 1980.

Marshak A., A. Davis, R. Cahalan, and W. Wiscombe, Bounded cascade models as non-stationary multifractals, *Phys. Rev. E*, *49*, 55-69, 1994.

Marshak, A., A. Davis, W. Wiscombe, and G. Titov, The verisimilitude of the independent pixel approximation used in cloud remote sensing, *Remote Sens. Environ.*, *52*, 71–78, 1995.

Meneveau, C., and K. R. Sreenivasan, Simple multifractal cascade model for fully developed turbulence, *Phys. Rev. Lett.*, *59*, 1424–1427, 1987.

Monin, A.S., and A. M. Yaglom, *Statistical Fluid Mechanics*, vol. 2, 683 pp., MIT Press, Cambridge, Mass., 1975.

Nakajima, T., and M. D. King, Determination of the optical thickness and effective particle radius of clouds from reflected solar radiation measurements, I, Theory. *J. Atmos. Sci.*, *47*, 1878–1893, 1990.

Parisi, G., and U. Frisch, A multifractal model of intermittency, in *Turbulence and Predictability in Geophysical Fluid Dynamics*, edited by M. Ghil, R. Benzi, and G. Parisi, pp. 84-88, North-Holland, New York, 1985.

Rybicki, G., and A. Lightman, *Radiative Processes in Astrophysics*, 382 pp., John Wiley, New York, 1979.

Stamnes, K., S.-C. Tsay, W. J. Wiscombe, and K. Jayaweera, Numerically stable algorithm for discrete-ordinates-method radiative transfer in multiple scattering and emitting layered media, *Appl. Opt.*, *27*, 2502, 1988.

Stephens, G. L., The transfer of radiation through vertically non-uniform Sc clouds, *Contrib. Phys. Atmos.*, *49*, 237–253, 1976.

Van de Hulst, H.C., *Multiple Light Scattering (Tables, Formulas, and Applications)*, vol. 2, 739 pp., Academic, San Diego, Calif., 1980.

Viscek, T., and A.-L. Barabási, Multi-affine model for the velocity distribution in fully turbulent flows, *J. Phys. A Math Gen.*, *24*, L845-L851, 1991.

Waymire, E., and V. J. Gupta, The mathematical structure of rainfall representations, 1–3, *Water Resour. Res.*, *17*, 1261-1294, 1981.

R. Cahalan, A. Davis, A. Marshak, and W. Wiscombe, NASA Goddard Space Flight Center, MC 913, Greenbelt, MD 20771. (e-mail: cahalan@clouds.gsfc.nasa.gov; davis@climate.gsfc.nasa.gov; marshak@climate.gsfc.nasa.gov; wiscombe@climate.gsfc.nasa.gov)

(Received May 9, 1995; revised September 5, 1995;
accepted September 5, 1995.)